Delft University of Technology

Single-Molecule Structure and Topology of Kinetoplast DNA Networks

He, Pinyao; Katan, Allard J.; Tubiana, Luca; Dekker, Cees; Michieletto, Davide

Important note
To cite this publication, please use the final published version (if applicable).
Please check the document version above.

Single-Molecule Structure and Topology of Kinetoplast DNA Networks

Pinyao He⊙,[1,2] Allard J. Katan⊙,[1] Luca Tubiana⊙,[3,4,5] Cees Dekker,[1] and Davide Michieletto⊙[6,7,*]

[1]*Department of Bionanoscience, Kavli Institute of Nanoscience,*
Delft University of Technology, 2629 HZ Delft, Netherlands
[2]*Jiangsu Key Laboratory for Design and Manufacture of Micro-Nano Biomedical Instruments,*
School of Mechanical Engineering, Southeast University, Nanjing 211189, China
[3]*Physics Department, University of Trento, via Sommarive, 14 I-38123 Trento, Italy*
[4]*INFN-TIFPA, Trento Institute for Fundamental Physics and Applications, I-38123 Trento, Italy*
[5]*Faculty of Physics, University of Vienna, 1090 Vienna, Austria*
[6]*School of Physics and Astronomy, University of Edinburgh,*
Peter Guthrie Tait Road, Edinburgh EH9 3FD, United Kingdom
[7]*MRC Human Genetics Unit, Institute of Genetics and Cancer,*
University of Edinburgh, Edinburgh EH4 2XU, United Kingdom

Kinetoplast DNA (kDNA) is a two-dimensional Olympic-ring-like network of mutually linked DNA minicircles found in certain parasites called trypanosomes. Understanding the self-assembly and replication of this structure are not only major open questions in biology but can also inform the design of synthetic topological materials. Here, we report the first high-resolution, single-molecule study of kDNA network topology using AFM and steered molecular dynamics simulations. We map out the DNA density within the network and the distribution of linking number and valence of the minicircles. We also characterize the DNA hubs that surround the network and show that they cause a buckling transition akin to that of a 2D elastic thermal sheet in the bulk. Intriguingly, we observe a broad distribution of density and valence of the minicircles, indicating heterogeneous network structure and individualism of different kDNA structures. Finally, we estimate the 2D Young modulus of the network to be orders of magnitude smaller than that of other 2D materials. Our findings explain outstanding questions in the field and offer single-molecule insights into the properties of a unique topological material.

I. INTRODUCTION

Kinetoplast DNA (kDNA) is one of the most fascinating naturally occurring genomes [1–7]. It is formed in the mitochondrion of unicellular parasites of the class kinetoplastida, and it is composed by an interlinked two-dimensional network of small DNA circles, or "minicircles," and larger DNA rings called "maxicircles." Maxicircles contain the genetic information for the synthesis of mitochondrial proteins, while minicircles display somewhat redundant genetic information and are mainly necessary to perform extensive RNA editing on the maxicircle mRNA [8]. The precise composition of the network depends on the organism; for instance, *Crithidia fasciculata* kDNA is contained within a 1 μm × 0.4 μm disk-shaped organelle and made of about 5000 minicircles (2.5 kb, or 850 nm, long) and 30 maxicircles (about 30 kb, or 10 μm, long). The mechanisms through which kDNA self-assembles and replicates are poorly understood [4,9–12].

The evolutionary benefit of a linked mitochondrial genome remains a major open question in trypanosome biology [9,13]. It has been speculated that the interconnected structure of linked rings provides genomic stability and a means to mechanically preserve genetic material, i.e., to avoid losing minicircles during cell division [9]. A common feature of kDNA is that it is found in the basal body, near the parasite flagellum. For this reason, it has also been speculated that the linkedness of the network may serve to provide mechanical stability to the organelle [6]. Taken outside the parasite, kDNA expands to assume a "shower-cap" buckled shape about 5 μm in size [14–16]. Once adsorbed onto a surface for electron microscopy (EM) or atomic force microscopy (AFM), kDNA stretches to an oval shape 8 μm × 10 μm in size and displays a thick border which is characterized by rosettes and brighter nodes [17–20].

In 1995, Cozzarelli and coauthors designed an elegant, albeit indirect, bulk method based on gel electrophoresis of digestion products to show that *C. fasciculata* kDNA topology is compatible with a two-dimensional hexagonal network where each ring is linked to other three minicircles, on average [21,22]. These results have also been recently independently confirmed using the same bulk method [23]. In spite of this, recent microscopy experiments indicate that kDNAs assume highly heterogeneous shapes, suggesting a broad spectrum of topologies [14].

Alongside experiments, computational and theoretical work have provided evidence that this type of linked network may be formed as a result of a percolation transition [23–25]. Beyond the percolation transition, overlapping rings form a system-spanning network of interlocking rings. At the onset percolation, the mean valence v, i.e., the number of rings that are linked to any one ring on average, was found to be three in simulations [25], in agreement with gel electrophoresis experiments [21].

Arguably, the minicircles acquire their valence *in vivo*, in a condition where the kDNA is under confinement. Given a minicircle number density $\rho \simeq 5000$ rings$/[\pi(0.5 \ \mu m)^2 0.4 \ \mu m] \simeq 15\,900$ rings$/\mu m^3$ and a radius of gyration of a minicircle $R_g \simeq l_p \sqrt{L/12 l_p} \simeq 60$ nm, one would expect a number of overlaps per minicircle $P = 4\rho/3\pi R_g^3 \simeq 14.4$. Even if only half of the overlapping minicircles became linked to each other via topoisomerase-mediated strand crossing [3] or the linking effectively occurred in 2D due to stacking and alignment [24,26], this overlapping number would still yield a valence much larger than $v = 3$ estimated by Cozzarelli [21]. These arguments suggest that the kDNA cannot be thought of as a gas of freely crossable rings and instead regulates its topology via, e.g., packaging proteins such as KAP [19] or by tuning the temporal and/or spatial activity of topoisomerases.

All of the quantitative evidence on kDNA network topology comes from indirect, bulk measurements [21–23], and recent microscopy work suggests that different kDNA networks have very different shapes and behaviors, suggesting heterogeneity in the self-assembly of this fascinating structure [14]. To shed more light into this, here we study *C. fasciculata* kDNA networks using high-resolution single-molecule AFM and molecular dynamics simulations. More specifically, we first quantitatively map the density of minicircles in the network as a function of their position and quantify the network structure by measuring its porosity. We also identify the characteristic rosettes at the rim of the network as originating from the localization of essential crossings between linked minicircles. Imposing a constraint on the size of the rim, we computationally show that the network undergoes a buckling transition that explains recent *in vitro* observations. Then, we employ steered molecular dynamics simulations to reconstruct the topology of the network at the single-molecule level. We, thus, obtain the full distribution of the valence in the network: We find it to be compatible with a mean valence of 3 but at the same time to display a broad distribution, suggesting heterogeneity in the network topology and across networks. Notably, our findings are not compatible with a perfect hexagonal network, thus refusing the classical model by Cozzarelli [21]. Finally, we discuss our findings in light of the work done on subisostatic floppy networks [27] and 2D elastic thermal sheets [28] and predict that the kDNA should display a 2D Young modulus much lower than that of other 2D materials such as lipid membranes and 2D mechanically interlocked structures.

II. RESULTS

A. The density of minicircles is not uniform

We perform dry, high-resolution AFM on *C. fasciculata* kDNA (TopoGen). A representative image, enlargements, and sketches are shown in Figs. 1(b)–1(e). We first notice
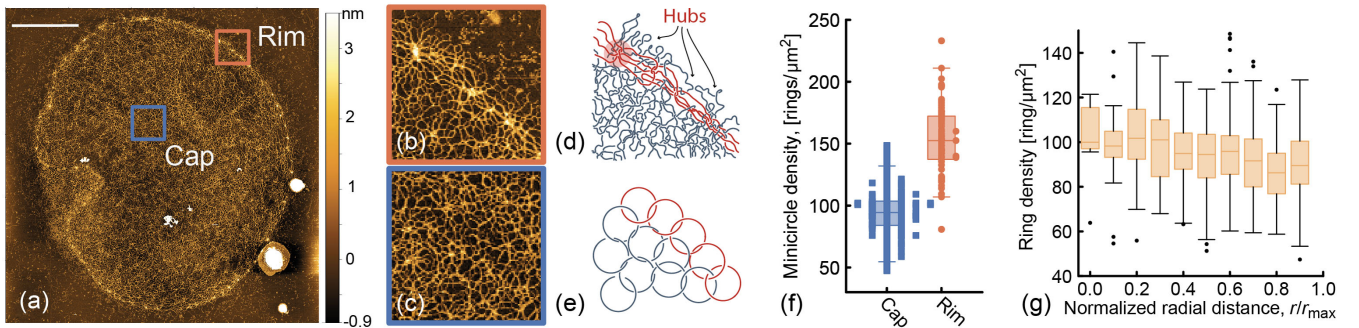
FIG. 1. (a) AFM images of kDNA from *C. fasciculata*. The scale bar is 2 μm, and the yellow color scale ranges from 0 (black) to 3.5 nm height (white). (b),(c) Enlargements of the rim and cap, respectively. (d) Sketch of the network of minicircles from (b) where we color code the minicircles forming the rim in red. (e) Simplified sketch where we schematically show that the network is formed by linked rings. This is not a one-to-one representation of (d). (f) Box plot of minicircle density in the cap and the rim of the network (obtained from selected regions and averaged across three kDNA networks). The rim density is computed by taking a circular region of radius $r = 100$ nm (about the size of a minicircle; see below) centered at the hubs. (g) Box plots of the density of minicircles as a function the distance from the center.

FIG. 2. (a) Examples of single rings used to compute the perimeter and radius of gyration of single minicircles. The scale bar is 500 nm. (b),(c) Enlargements of minicircles with supercoiledlike (b) and open (c) conformatio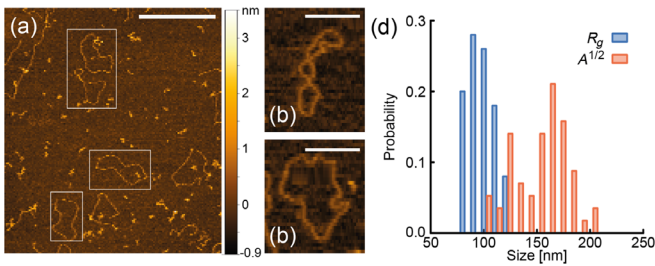ns. Scale bars are 250 nm. (d) Size of the minicircles, computed as the radius of gyration of the AFM traces, R_g, and the square root of the area, $A^{1/2}$. We find a mean $R_g = 101.3 \pm 10.8$ nm, in line with Ref. [29] reporting $R_g = 109$ nm for 2.6-kb-long plasmids, and mean $A^{1/2} = 154.4 \pm 22.5$ nm.

that the networks display fluctuations in the density of minicircles (bright and dim areas within the kDNA "cap"). At the edge of the networks, we notice bright and regularly spaced nodes along its edge, as previously reported [18–20] [see Figs. 1(b)–1(e)]. To quantify the density of minicircles in different regions of the kDNA, we first measure the volume of isolated minicircles outside the kDNA network (see also Fig. 2). These provide an internal control in our experiments, as minicircles outside the kDNA network are subjected to the same experimental artifacts (e.g., sample dehydration) as the ones within the network. In turn, we obtain an average volume for the single minicircles I_{mc} which we use to normalize the volume found in regions within the kDNA. We then randomly sample selected regions within the cap of the network and normalize their total volume $I(r)$ by I_{mc}. The quantity $\rho(r) \equiv I(r)/(I_{mc}A)$, where A is the area of the sampled region, is the number density of minicircles at location r in the image.

By averaging over four independent kDNA networks (see Supplemental Material [30] for raw images), we find that there are $\rho = 94 \pm 17$ rings/μm^2 in the cap [see Fig. 1(f)]. Given that the mean short and long axes of our kDNAs are $l = 7.8$ μm and $L = 9.1$ μm, respectively, we find a corresponding total number of minicircles $N_{tot} = \rho \pi l L = 5296$. Considering the limits of the pixel resolution and the assumptions made for the conversion of signal intensity to DNA mass, this number is in excellent agreement with that reported in the literature, i.e., 5000 [21] for C. fasciculata kDNA. It should be highlighted that we could have arrived at a similar value of ρ by simply assuming that the network is formed by 5000 rings uniformly distributed in the network; however, using our method, we (i) verify independently that the network has around 5000 rings and (ii) develop a way to measure ring density as a function of position r in the kDNA. By applying the same method to the "hubs" along the rim of the kDNA—which we define as the region within one

minicircle size ($r = 100$ nm; see below) from the center of the brightest nodes—we find that the average ring density is significantly larger at the rim, with mean $\rho_{rim} = 153.1 \pm 27.0$ rings/μm^2 [see Fig. 1(b)].

We then ask if there is a dependence of minicircle density as a function of the position in the network. We sample about 200 small regions in four different kDNA networks and compute $\rho(r)$ as above. We then plot this as a function of the radial distance $r = |r - r_c|$ from the center of the network. We discover that the density displays a smooth decrease by approximately 13% from the center to the periphery [Fig. 1(d)]. Since a uniformly filled disk that is stretched isotropically still displays a uniform mass distribution, we argue that the observed density gradient is a feature of the network rather than an artifact of the imaging method. We hypothesize that this density gradient may be locked in at the end of replication—which occurs at antipodal points positioned outside the kDNA and in relative rotation with respect to the kDNA disk in C. fasciculata [4]. The gradient in minicircle density suggests that the topology of the kDNA may not be uniform and that minicircles in the middle of the cap may be more connected than the ones at the periphery (excluding the rim). The density gradient and the difference between DNA density in cap and rim have not been reported nor quantified before, and we argue that these are potentially important to account for in future models of kDNA self-assembly [21,23–25,31].

B. Estimating the valence of minicircles

Based on our measurement of minicircle density within the cap, we now estimate the valence v of the minicircles, i.e., the number of minicircles that are linked to any one minicircle. To do this, we first compute the minicircle average size by tracing the contour of DNA rings found outside the network [in Fig. 2(a), we show examples of minicircles used for this analysis]. We find that isolated minicircles have a mean contour length of $L_c = 791 \pm 66$ nm and a mean radius of gyration $R_g = 101.3 \pm 10.8$ nm, which is in good agreement with the size measured by AFM of DNA plasmids of similar length absorbed in 2D [32]. Since we observe heterogeneous conformations displaying plectonemiclike writhe [Fig. 2(b)], we also compute the area of the minicircles and notice that it displays a broader distribution, compatible with the presence of writhing and open minicircles in the AFM images [Figs. 2(b)–2(d)]. From the number density of minicircles per unit area ρ and their average size R_g, we estimate that the number of overlapping minicircles in the flattened kDNA is $P \simeq \rho \pi R_g^2 \simeq 3$ (valid for isotropic and randomly shaped minicircles). This number is about fivefold smaller than the number of overlaps expected *in vivo* (where we recall that the kDNA is contained within a disk 1 μm in diameter and 0.4 μm in height) but is compatible with the average valence $v \simeq 3$ measured by Cozzarelli [21].

At the rim, we may use an effectively larger minicircle density, yielding $P \simeq \rho_{rim} \pi R_g^2 \simeq 4.8$, in turn suggesting a

larger valence of the minicircles at the hubs. However, we note that the minicircles at the rim are stretched, in turn increasing their R_g and potentially their real valence. In the next section, we characterize the minicircles at the rim in more detail.

Finally, we note that the R_g we measure from the 2D absorbed minicircles is typically larger than the R_g they would assume in bulk [33]. In the extreme case that they assume the shape of ideal loops, we recall that we would expect $R_g \simeq 60$ nm. In turn, we would expect a valence of about 1 for ring density $\rho \simeq 95$ μm^2. On the other hand, we know that *in vivo* the kDNA is packaged at much larger density, which, therefore, increases the maximum valence that each minicircle can reach. Indeed, if every minicircle were linked to every overlapping neighbor, we would expect $v \gtrsim 10$. In spite of this, one should bear in mind that DNA minicircles cannot link without the presence of (type 2) topoisomerase; thus, its activity within or at the periphery of the network appears to be critical to regulate the catenation of the network [9,34,35].

We should note that, importantly, the topology of the network is unchanged from its native, physiological state *in vivo* and that the density of minicircles measured in the previous section, together with their size, is intimately related to the inherent network topology. If the minicircles had a larger valence, we would inevitably expect a correspondingly larger DNA density due to the reduced expansion of the network when stretched. The fact that our networks have the same topology that they have *in vivo* is a key feature that connects our measured structural parameters to the physiological situation.

C. The kDNA hubs are sites of essential crossings between linked minicircles

As mentioned above, a feature that stands out from the AFM images is the rim, formed by nodes (or hubs) connected by clear DNA tethers [Figs. 3(a) and 3(b)]. By enlarging these features, one can appreciate that these nodes are formed when several minicircles come together into so-called "rosettes" [20] [Figs. 3(a) and 3(b)].

The average distance between nearest nodes in the network is close to that of a minicircle pulled taut, i.e., $L_t = 0.5 \times 2500$ bp $\times 0.34$ nm/bp $= 425$ nm [Fig. 3(c)]. Additionally, by directly measuring the density of strands in a circular region with radius $r = 100$ nm (equal to that of a minicircle in equilibrium outside the network) and centered at the nodes, we find that the average number of overlapping minicircles per hub is $P_{hub} = 4.7 \pm 0.8$, which should be compared with $P_{cap} = 2.9 \pm 0.4$ found in the cap [Fig. 3(d)]. This may still be an underestimate, as the minicircles at the rim are stretched and their overlap number may, thus, be larger. Our images [see Figs. 3(a) and 3(b)] also suggest that nearest nodes are directly connected by single minicircles, which are, therefore, redundantly linked. When minicircles are stretched due
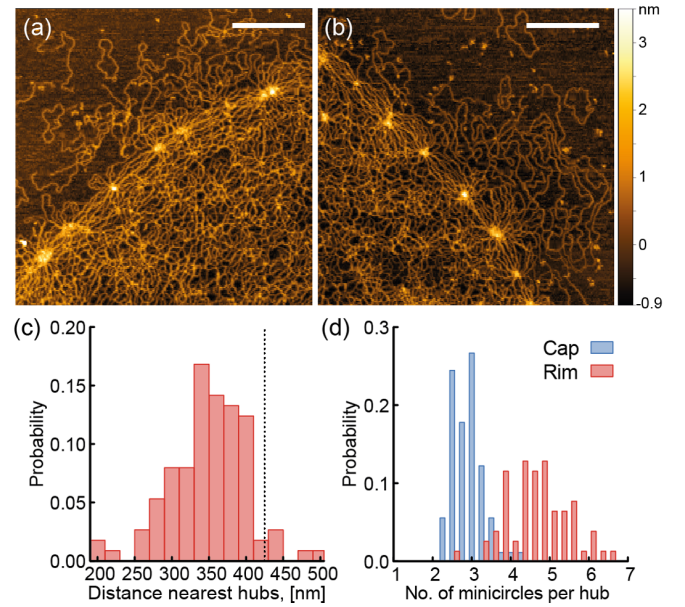

FIG. 3.   (a),(b) Enlarged portions of kDNA showing hubs at the periphery. Scale bars are 500 nm. (c) Distribution of distances between nearest hubs. The dashed vertical line represents the diameter of a minicircle if pulled taut, i.e., $1/2 \times 2500$ bp $\times 0.34$ nm/bp $= 425$ nm. (d) Distribution of a number of overlapping minicircles in the cap and in the hubs.

to the kDNA being absorbed, the essential crossings between minicircles become localized in hot spots [36], forming the hubs. In the bulk, we expect the minicircles to relax and the hubs to disappear, although a rim with higher DNA density can still be visualized [14].

The reason why *C. fasciculata* kDNA displays a larger density of minicircles at the rim may be due to its replication mechanism, as newly replicated minicircles are added at the periphery from the antipodal points located just outside of a rotating kDNA network [22,34]. We also recall that, *in vivo*, the kDNA is compressed in a disk of diameter of 1 μm, while it reaches approximately 10 μm when fully adsorbed. This approximately tenfold compression *in vivo* effectively reduces the distance between nodes, and we, thus, expect the essential crossings to be within 1 R_g of each other. This redundancy in the number of links is akin to that of replicating kDNA networks [22], and we, thus, argue that the edge of the network could be made by newly replicated minicircles.

D. Simulations of kDNA with a constrained rim explain the buckling seen in bulk

Our data suggest that the minicircles at the rim are both redundantly linked and stretched upon adsorption on the mica. In the bulk, these minicircles tend to relax to their equilibrium diameter, i.e., reducing their diameter from $\simeq 350$ nm to $\simeq 200$ nm. This yields an $\simeq$ twofold decrease in perimeter length as the essential crossings become
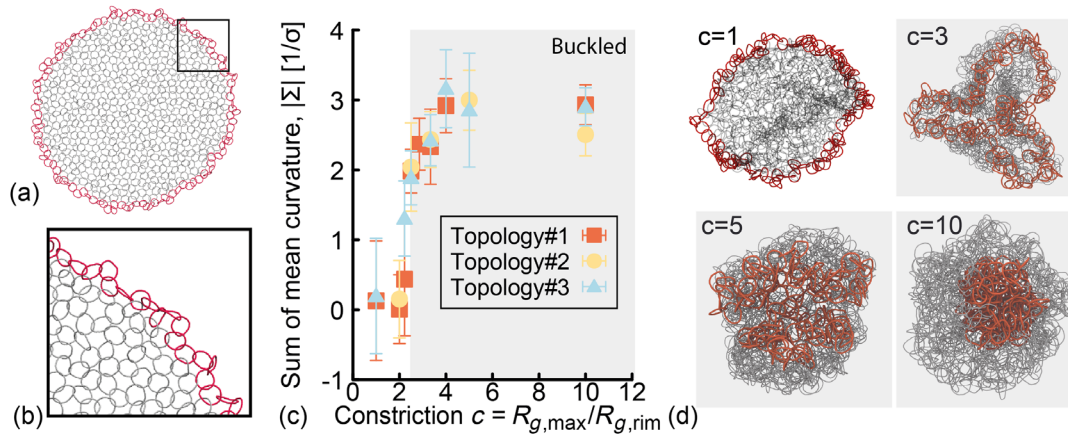
FIG. 4. (a) An *in silico* kDNA with hexagonal structure of rings. The border is highlighted in red. (b) Enlarged portion of (a) showing the hexagonal lattice linkages. See Supplemental Material [30] for details on how the network is built. (c) Absolute value of the sum of the mean curvature of the triangular mesh, $|\Sigma|$, calculated by joining the center of mass of the rings and plotted as a function of the constriction $c = R_{g,\max}/R_{g,\text{rim}}$. In these simulations, $R_{g,\text{rim}}$ is user defined and steered using a harmonic potential. The plot shows an abrupt buckling transition. Different symbols correspond to different network topologies chosen by random linking of neighboring rings while preserving the hexagonal structure. (d) Snapshots of the network at four different values of constriction c.

delocalized due to the minicircles' entropy, in turn leading to a certain degree of overlap [36]. If we thus treat the perimeter of the kDNA as a polycatenane (a polymer made of linked rings [37,38]), it is clear that a reduction in length leads to a decrease in its radius of gyration R_g. Thus, we can study the behavior of the kDNA under a variable degree of constraint on the length of its perimeter (due to minicircles relaxing to equilibrium conformations) by imposing a constraint on the size (radius of gyration) of the rim.

To do this, we simulate a circular patch of an hexagonal (in line with Refs. [21,31]) network and constrain its border to have a radius of gyration $R_{g,\text{rim}}$ different from that assumed when the patch is completely planar, called $R_{g,\max}$. We consider a system made of $n = 604$ rings, each made of $m = 60$ self-avoiding beads connected by finitely extensible nonlinear elastic (FENE) springs [see Figs. 4(a) and 4(b) and Supplemental Material [30] for details]. For computational efficiency, we consider semirigid rings, with persistence length $l_p = 120$ beads, but we expect a similar result for flexible rings; as we see below, the location of the buckling transition is expected to be mainly dependent on the ratio of the 2D Young modulus and the bending stiffness. The network is constructed by placing the rings on the nodes of a circular patch of hexagonal lattice [39] and then linking each ring with its neighbors by randomly choosing between a +1 and a −1 Hopf link. We identify the border of the network as the set of rings having only two neighbors or being directly linked to a ring having two neighbors only. We constrain the radius of gyration R_g of the rim to a user-defined value $R_{g,\text{rim}}$ with an additional harmonic potential in the Hamiltonian:

$$V_{\text{constr}} = K(R_g - R_{g,\text{rim}})^2. \tag{1}$$

We then simulate the equilibrium behavior of three different network topologies (distinguished by the sign of the linking numbers between neighboring rings) for different values of $R_{g,\text{rim}}$ via Langevin dynamics in LAMMPS [40] (see Supplemental Material [30] for details).

We highlight that this approach is agnostic to the precise geometrical arrangement and topology of the minicircles at the periphery. It effectively captures the fact that stretched minicircles return to their equilibrium size and shrink the periphery of the network when lifted from the mica. Since the distance between localized essential crossings is $\simeq 400$ nm (Fig. 3) and the equilibrium diameter of isolated minicircles $\lesssim 200$ nm (Fig. 2; note that minicircles in the network have smaller R_g than isolated ones), we estimate a reduction in circumference > 2 accompanied by a similar reduction of its R_g. Thus, by using a continuously varying constraint on R_g, we can study the behavior of the network under different levels of shrinkage.

To quantify the equilibrium geometrical properties of the network, we first map the hexagonal lattice of rings to a triangular mesh with edges connecting the center of mass of half of the rings and then compute the mean curvature as [41]

$$\Sigma = \sum_{i=1}^{N} \frac{1}{2}(K_{1,i} + K_{2,i}), \tag{2}$$

where $K_{1,i}$ and $K_{2,i}$ are the principal curvatures at facet i (see Supplemental Material [30] for the details). The results, reported in Fig. 4(c), show that, when the constraint at the perimeter is $R_{g,\max}/R_{g,\text{rim}} > 2$, the equilibrium conformations display a buckled, "shower-cap" shape, as seen in experiments [14] [see Fig. 4(d)]. Interestingly, the
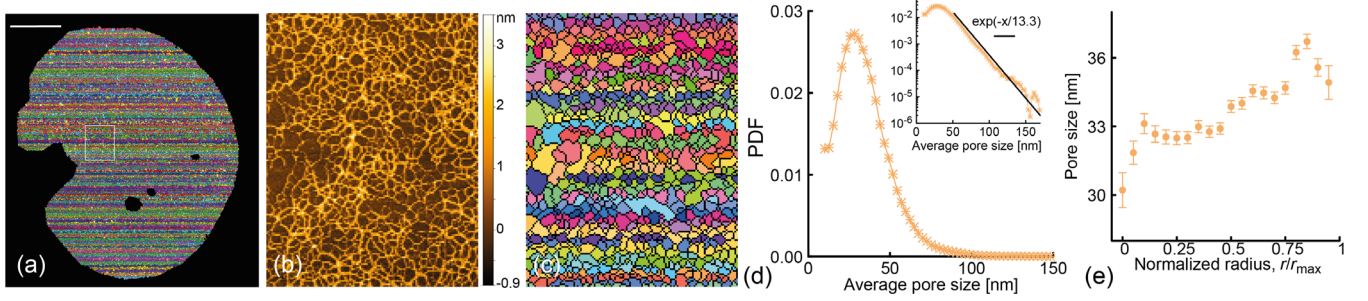
FIG. 5. (a) Morphological segmentation of the AFM image show in Fig. 1(a). The scale bar is 1 μm. (b) An enlarged region showing side by side the AFM picture and in (c) the result of morphological segmentation. (d) Probability density function (PDF) of mesh size. The inset shows a log-linear plot of the same PDF, with an exponential decay reported as a guide for the eye. (e) Average pore size as a function of the radial distance from the center of the network.

absolute mean curvature $|\Sigma|$ increases abruptly from 0 (saddlelike surface) to $\simeq 1\sigma^{-1}$ (buckled) and eventually to $\simeq 3\sigma^{-1}$ (shower cap).

We highlight that the buckling transition occurs close to the constriction value $R_{g,\max}/R_{g,\mathrm{rim}} \simeq 2$, which is the value we expect in the kDNA due to the shrinkage of the minicircles as they relax from fully stretched ($\simeq 400$ nm) to relaxed ($\lesssim 200$ nm). Thus, our simulations strongly suggest that the buckling behavior of the kDNA observed *in vitro* is mainly determined by how the rim is self-assembled *in vivo* rather than by the kDNA internal (cap) topology.

E. Mesh size distribution

Having quantified the distribution of minicircles in the network, we now quantify its mesh size. Given that the minicircle density is around $\rho = 94$ rings per μm^2, the interminicircle separation is $\lambda = 1/\sqrt{\rho} = 103$ nm. In turn, we can estimate the mesh size as $\xi = |\lambda - 2R_g| \simeq 100$ nm (recall that $R_g = 101.3$ nm; see Fig. 2).

To quantify the mesh size more precisely, we employ morphological segmentation [42]. We first manually remove both imaging artifacts and the rim from within the region of interest [see Fig. 5(a) to be compared with Fig. 1(a)]. We then apply morphological segmentation to obtain a map of watershed basins, as shown in Figs. 5(a)–5(c). We then measure the area of each basin a and estimate their size $\xi = \sqrt{a}$. We find that the values of pore sizes are broadly distributed and range between 10 and 200 nm with a peak (median) around 20 nm and mean $\xi = 34.0 \pm 16.6$ nm.

The distribution of mesh sizes appears to follow an exponential behavior for values larger than 50 nm [Fig. 5(d)]. These values are small compared with the typical 100–500 nm of agarose gels and closer to those of DNA nanostar gels [43].

Interestingly, by computing the distance of all the basins from the center of the network, we observe that the average pore size increases toward the periphery [Fig. 5(d)]. This is

in line with our previous finding that the DNA density decreases toward the periphery. More specifically, we find pore sizes around 30 ± 0.7 nm within the center and around 35 ± 0.7 nm near the periphery (where the redundantly rim is excluded). We note that these values are smaller than the crude calculation we make above ($\xi \simeq 100$ nm), which is valid only for perfectly rigid minicircles. This is most likely due to the fact that the minicircles are writhing onto themselves, thereby yielding smaller pore sizes overall.

Finally, we note that, in a lattice of rigid rings where every overlap is a link, one can map the number of pores (basins in the morphological segmentation) to the number of rings and their valence as $N_{\mathrm{pores}} > N_{\mathrm{rings}}(1 + v/2)$. With flexible rings and nonconnected overlaps, we expect more pores formed. We can, therefore, set an upper bound on the valence in the networks that we analyze: $v < 2(N_{\mathrm{pores}} - N_{\mathrm{rings}})/N_{\mathrm{rings}}$. From the morphological segmentation, we find $N_{\mathrm{pores}} = 19644 \pm 2404$, in turn implying $v < 6$. This large upper bound is likely due to overlaps which do not result in linking yet still create mesh pores. Arguably, and contrary to common chemically cross-linked gels, the observed pores only mildly contribute to the network elasticity, as some overlaps can be easily resolved by pulling the rings past each other.

F. AFM-steered simulations

Despite the high-resolution AFM images, it is still challenging to identify single minicircles inside the cap of the network, and even less clear is to identify over- and undercrossings between chains [see, for example, Fig. 5(b)]. Because of this, it is impossible to unambiguously compute the topology of the network. More specifically, we aim to quantify the distribution of linking number Lk (defined as the number of times minicircles wrap around one other) and the valence v (defined as the number of minicircles that are linked with any other one). To measure these, we perform molecular dynamics simulations steered by our AFM data, with the aim of obtaining
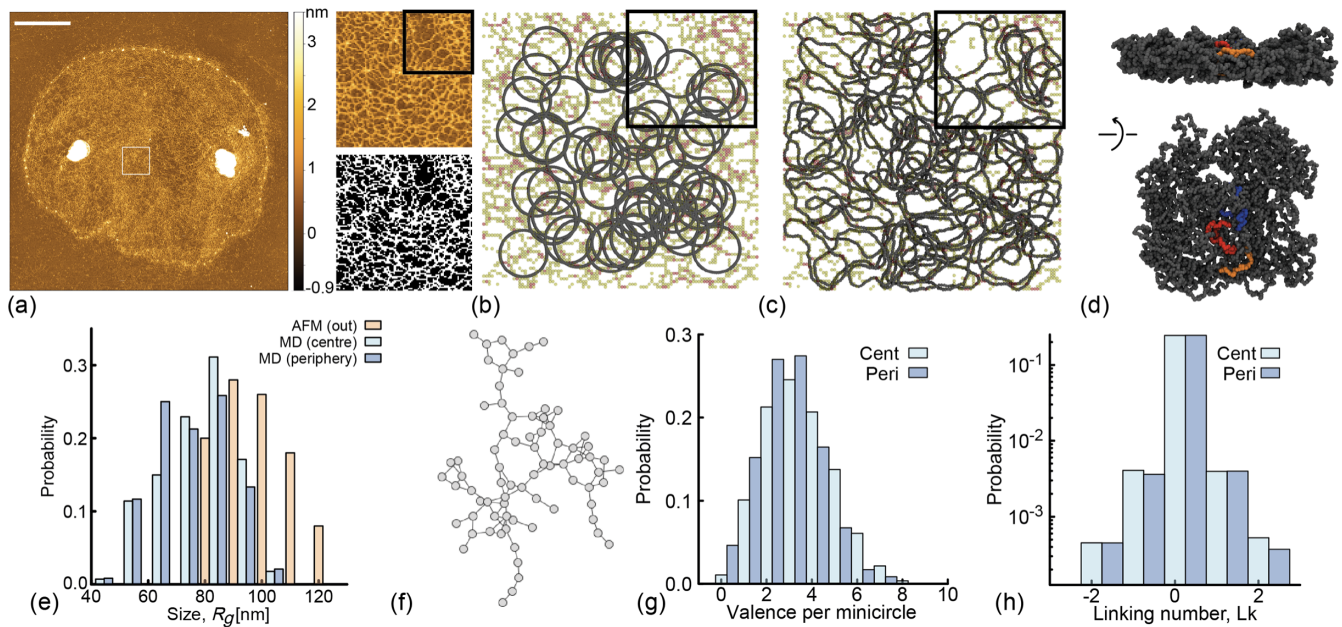
FIG. 6. (a) Figure showing a kDNA image (the scale bar is 2 μm) and an enlarged 1 μm² region with the corresponding thresholded image (black and white). (b) Starting configuration of the AFM steered MD: 90 rings are placed randomly in a quasi-two-dimensional simulation box. Phantom beads (yellow, orange, and red in the figure) are static and act as Gaussian attracting basins. (c) At the end of the MD simulation, we obtain ensembles of conformations that capture the correct length and size of minicircles, display no ambiguous crossings with other rings. and are compatible with the underlying AFM image. (d) Snapshot of the resulting network after having removed the slab confinement. (e) Distributions of R_g of the minicircles from AFM (picked from outside the kDNA) and of the simulated ones (both from the center and periphery). (f) Network representation of (d), where each node is a minicircle and an edge between nodes represents that they are linked. Our simulated networks typically have all the nodes in one large connected component. (g) Distribution of valence, showing that the central minicircles are on average more connected than the peripheral ones. (h) Distribution of linking number, showing that the most linked pairs are singly linked, and about 10% of them are doubly linked.

XYZ coordinates of the DNA segments making up minicircles within the network.

To do this, we select a 1 μm × 1 μm region (ROI) within the kDNA cap [Fig. 6(a)]. We then binarize the image by selecting the pixels whose intensity is larger than the mean background intensity plus 3 standard deviations. We then use the binarized image as a mask on the original ROI to extract the intensity of the pixels corresponding to DNA strands in the AFM image. These pixels are transformed into three types of phantom (nonsterically interacting) and static (nonmoving) beads which attract the simulated DNA rings (see Supplemental Material [30] for details of the procedure and of the potentials used).

Molecular dynamics simulation is initialized by placing M perfectly circular minicircles within the 1 μm² region [see Fig. 6(b)]. Each minicircle is modeled as a semiflexible bead-spring polymer, where each bead is $\sigma = 10$ nm (the AFM pixel resolution); in turn, the 2.5-kb-long or 850-nm-long minicircles are represented by 85 beads and a persistence length $l_p = 5\sigma = 50$ nm. The interaction between rings is modeled via a soft potential. The simulation is performed within a slab confinement in the z direction with height $h = 3.0\sigma$. The steered simulation is split in three parts: (i) equilibration, (ii) steering, and

(iii) resolving crossings. In part (i), we homogenize the distribution of rings in the system. We, thus, set a low-energy barrier for crossing, and the rings are let to equilibrate and to cross each other. In part (ii), we steer the rings' coordinates by turning on attraction between the beads forming the DNA rings and the "phantom" beads obtained from the AFM image [see Figs. 6(b) and 6(c); see Supplemental Material [30] for details]. This phase ensures that the simulated minicircle assumes conformations that are compatible with the underlying AFM image. In part (iii), we resolve overlaps between rings by ramping up the height of the soft repulsive potential between polymer beads. The final output of this procedure is an ensemble of minicircle coordinates with fully resolved overlaps, i.e., well-defined over- and undercrossings, and whose 2D projections are compatible with the underlying AFM image we started from [Figs. 6(c) and 6(d)].

Motivated by our previous findings, we perform the procedure just described in a region near the center and one at the periphery (rim excluded) of the kDNA. In the former, we initialize $M = 90$ rings, while at the periphery we initialize $M = 80$ rings within the 1 μm² ROI, in line with the values of minicircle density reported in Fig. 1. To benchmark our steered simulations with experiments, we

first compare the distribution of ring sizes. We find that the distribution is close to the one obtained from isolated kDNA minicircles in the AFM images (Fig. 2) with the caveat that the simulated rings display a broader size distribution and a smaller mean, which is reasonable given that they are in dense conditions, whereas the AFM minicircles over which we compute the R_g are isolated, outside the network. The experimental mean is $R_g = 101.3 \pm 10.8$ nm, while the simulations give $R_g = 71 \pm 15$ nm at the center and $R_g = 72 \pm 15$ nm at the periphery [Fig. 6(f)], closer to the value estimated for ideal chains ($R_g \simeq 60$ nm).

From the ensemble of conformations with resolved overlaps, we can unambiguously compute the Gauss linking number between pairs of minicircles as

$$Lk = \frac{1}{4\pi} \oint_{\gamma_1} \oint_{\gamma_2} \frac{(\mathbf{r}_1 - \mathbf{r}_2) \cdot (d\mathbf{r}_1 \times d\mathbf{r}_2)}{|\mathbf{r}_1 - \mathbf{r}_2|^3}, \quad (3)$$

where $\mathbf{r}_i$ represents the 3D coordinate of curve γ_i. We, thus, define a linking matrix $Lk(i,j)$ where each entry is the number of times ring i is linked to ring j. Additionally, we define the valence of ring i as $m_i = \sum_j \theta[|Lk(i,j)|]$, where $\theta(x) = 1$ if $x > 0$ and 0 otherwise. Interestingly, we find that the distribution of the valence depends, albeit weakly, on the distance from the center of the network. In the more central ROI, we find a mean valence $\langle m_{\text{cen}} \rangle = 3.1 \pm 1.5$, while in the more peripheral region we find $\langle m_{\text{per}} \rangle = 2.5 \pm 1.3$ [Fig. 6(e)]. Furthermore, we measure the distribution of linking number $lk = Lk(i,j)$ across all pairs and find that, among those that are linked, the majority are singly linked, around 10% doubly linked, and less than 1% triply linked.

These numbers are in good agreement with the bulk, indirect measures in Ref. [21], whereas here we can provide a single-molecule quantification. Importantly, our method does not assume *a priori* an ordered lattice arrangement of the rings. Indeed, we find that they form connected, percolating components with valence 3 even in the absence of a precise hexagonal lattice structure [Fig. 6(f)]. Instead, we find a broad distribution of valences which overall retain the percolating nature of the structure. Our results, thus, confirm that the kDNA minicircles have on average valence 3, as found in Ref. [21], but they also indicate a broad valence distribution and no crystalline order.

G. Elasticity of kDNA as a subisostatic network

In light of our results, kDNAs can be thought of as 2D elastic networks with nodes (the minicircles) that have valence around 3, on average. In general, a network is said to be isostatic [27] when the number of constraints matches the number of degrees of freedom. For 2D networks, the critical isostatic coordination number is $v_c = 4$. Thus, the kDNA is a subisostatic (floppy) network, with valence comparable to that of other biological networks, such as

collagen [44]. The difference with collagen is that the bonds between nodes are not made by stiff fibers but are made by the linkages between minicircles, and their stiffness is approximately (at least for small strain) that of an entropic spring with constant $\kappa_0 = 3k_B T / R_g^2$. Subisostatic networks display soft modes that cost zero energy even when weakly strained [45] and undergo stiffening when stretched beyond a critical strain $\gamma_c(v)$ [44]. For strains $\gamma > \gamma_c$, we can estimate the bulk (area) stretch modulus as [44,46]

$$Y = \frac{5}{48} \rho \kappa_0 R_g^2 (v - v_c(\gamma)) \simeq 0.1 \frac{\text{pN}}{\mu\text{m}}, \quad (4)$$

where $v_c(\gamma)$ is the effective critical valence as a function of the strain. For the purpose of this estimate, we take $v - v_c(\gamma) \simeq 1$. In other words, we expect that it would take a modest force, around 3 pN, to stretch or compress a flat kDNA by 10%. We note that this calculation does not account for the redundantly linked and denser rim around the network. The bending rigidity can then be approximated as $\kappa_{\text{bend}} \simeq Y(2R_g)^2 \simeq 3 \times 10^{-21}$ J, with $2R_g$ about the average thickness of the kDNA.

The bending rigidity κ was also recently estimated using microfluidic constriction experiments and, in analogy with vesicle deformation, it was found to be $\kappa = 1.8 \times 10^{-19}$ N m [14]. However, the combination of in-plane and out-of-plane deformations in kDNA is expected to be different from that of vesicles, and, more importantly, we expect drastically different area stretch modulus. Lipid bilayers are liquidlike compositions of small molecules with approximately nanometer thickness and display large stretch moduli, $Y \simeq 0.1$–1 N/m [47], and equally large bending stiffnesses $\kappa \simeq 10^{-18}$ N m. In contrast, kDNA is made of 2.5-kbp-long DNA rings with an average size $R_g \simeq 100$ nm; furthermore, the density of material inside the kDNA is low compared with lipid bilayers, rendering the structure much easier to deform both in plane and out of plane. For these reasons, we expect the stretch modulus and bending stiffness of kDNA to be widely different from that of vesicles. In fact, according to Eq. (4), we expect these to be 2–3 orders of magnitude smaller. A clear complication of this picture is that kDNA networks in the bulk have undergone a buckling transition driven by the rim. This buckling may yield longer autocorrelation times of kDNA shapes (e.g., anisotropy) and shows fast, subsecond rearrangements which are more in line with far smaller and more flexible molecules [14].

Furthermore, we note that the buckling behavior of a 2D elastic thermal sheet is typically controlled by the dimensionless Föppl–von Kármán number $v_K = A/h^2$, where A is the area of the sheet and h its height. The parameter v_K can also be expressed in terms of the 2D Young modulus and bending rigidity as $v_K = YR^2/\kappa$, where R is a characteristic linear dimension of the system. Taking h

to be the diameter of minicircles in their relaxed state *in vitro*, we obtain for kDNA networks $v_K \simeq 1700$, which is far lower than other 2D materials (for instance, graphene has 10^9, being extremely thin). In this respect, kDNA is considered to be "thick" and, therefore, easily stretchable or compressible before buckling. In the "thin" limit, buckling occurs before any in-plane deformation.

The competition of compression and bending moduli gives rise to a natural length scale called "thermal length scale" which dictates the behavior of 2D elastic thermal sheets [28,48]. This length scale is found as

$$l_{\text{th}} = \sqrt{\frac{16\pi^3 \kappa^2}{3 k_B T Y}}. \tag{5}$$

When compression deformations are larger than l_{th}, it is more energetically favorable for a 2D elastic sheet to buckle out of plane. By using the values of Y and κ found above, we obtain a thermal length scale $l_{\text{th}} \simeq 1.8\ \mu\text{m}$. This value may be interpreted as the amount of compression needed for the network to buckle. Interestingly, the ratio of maximum radius of the kDNA to this thermal length scale is $R_{g,\text{max}}/l_{\text{th}} = 2.5$, which is in the buckled phase [see Fig. 4(c)]. This implies that the buckling behavior of kDNA is well described by the physics of 2D elastic thermal sheets and that, as we discuss above, the properties of the nodes at the rim are such that their relaxed state induces an in-plane compression beyond the thermal length scale of the network l_{th}, thereby inducing buckling. We argue that kDNA networks with different replication mechanisms may not display redundantly linked, stretched minicircles at the periphery, and are therefore expected not to buckle when in solution.

III. CONCLUSIONS

Overall, our study is the first to perform a quantitative analysis of single-molecule data on the structure and topology of *C. fasciculata* kinetoplast DNA networks. While previous works used indirect methods to obtain the kDNA topology [21], a single-molecule characterization of kDNA structure and topology did not exist.

We have employed high-resolution AFM, quantitative image analysis, and MD simulations to discover that the kDNA does not display a uniform DNA density, but instead it has more minicircles in the middle of the network than the periphery (Fig. 1). On average, we find about 95 minicircles per μm^2 in the cap of the network and 140 minicircles per μm^2 at the rim. Additionally, we have used morphological segmentation to quantify the pore size of the network (Fig. 5) and found that the mesh size is smaller in the middle (about 30 nm) compared with the periphery (about 36 nm). We note that, since the topology of the kDNA is unchanged during its extraction, our measurements capture its *in vivo* topology, too, and that this is

intimately linked to the DNA density we measure *in vitro*. For instance, if the minicircles had a larger valence, the network would undergo a smaller extension, reflected in a larger DNA density when deposited on the mica.

By noticing that the minicircles at the nodes appear stretched under AFM (also seen in previous EM [20] and AFM [18] images), we argued that, when not adsorbed onto a surface, the rim should shrink by $\simeq$ twofold, due to the entropic elasticity of the minicircles. Motivated by this, we simulated the behavior of a chainmail of linked rigid rings under varying degrees of constraint on the size $R_{g,\text{rim}}$ of the border and observed a buckling transition when $R_{g,\text{rim}}$ was set to be around 2.5–3 times smaller than that of the fully flat kDNA (Fig. 4). The buckling transition seen around $R_{g,\text{max}}/R_{g,\text{rim}} \gtrsim 2$ is in good agreement with the expected entropic shrinking of the kDNA in bulk and, thus, explains the stable "shower-cap" buckled shape recently seen in confocal microscopy [14,15]. Both our experiments and simulations agree with the calculation of the thermal length scale for kDNA being [Eq. (5)] $l_{\text{th}} \simeq 1.8\ \mu\text{m}$; this is around 2.5 times smaller than the radius of fully flat kDNA, and it marks the transition where buckling (out-of-plane) deformations are favored over compression (in-plane) deformations.

Finally, we have used steered molecular dynamics simulations to obtain ensembles of ring conformations that are compatible with the DNA distributions in the AFM images and can resolve certain topological ambiguities that cannot be resolved in the AFM image. Using these simulations, we have independently measured the valence of the minicircles in the network and found that it displays a broad distribution with a mean around 3. This finding is in remarkably good agreement with the measures by Cozzarelli [21] in spite of the fact that they are obtained in two completely different methods. Differently from the indirect, bulk quantification of the network topology done in the past, our high-resolution quantitative imaging allowed us to discover that the topology and connectivity of the network (i) is heterogeneous and broadly distributed and (ii) depends on the distance from the center of the network. It would be interesting in the future to understand more about the mechanisms leading to this gradient. Notably, our high-resolution and MD approach yielded networks that do not resemble perfect hexagonal arrangements but are instead random (Fig. 6). In the work of Cozzarelli [21], the hexagonal arrangement model was imposed due to the assumption of a perfectly two-dimensional network. We argue that this approximation is too stringent and that the percolating nature of the kDNA can be achieved also by allowing rings to randomly link at the right density [24,25].

We note that, in the language of 2D random networks, a valence (or coordination number) $v = 3$ is below the isostatic value [27], that for 2D networks is $v_c = 4$. This renders the kDNA a subisostatic, floppy network with soft (zero energy) modes and zero stress response at strains γ

below a critical $\gamma_c(v)$ [45]. At the same time, and although kDNA networks may resemble suspended membranes or lipid bilayers, they display a highly unusual structure, made of DNA minicircles that are thousands of base pairs long. More specifically, compared with lipid bilayers, kDNA displays a lower density and larger thickness. For this reason, we expect its material properties to be markedly different from that of lipid membranes, which are essentially incompressible and cannot sustain stretching beyond approximately 5% [47]. Indeed, the estimated stretch modulus $Y \simeq 0.1$ pN/μm [Eq. (4)] and its bending stiffness $\kappa \simeq 1$ pN nm are both thousands of times smaller than those of lipid membranes.

It is perhaps more interesting to compare the kDNA properties with synthetic mechanically interlocked networks (MINs) [49], woven and unwoven polymers [50], and DNA origami [51]. To make a fair comparison, we divide the 2D Young modulus by the thickness of the surface, $h \simeq 170$ nm, to obtain $E \simeq 0.6$ pN/μm$^2 = 600$ Pa. This is orders of magnitude smaller than those measured for woven and unwoven polymer surfaces ($\simeq$GPa) [50], auxetic DNA origami ($\simeq 1$ GPa) [51], and MINs ($\simeq 600$ MPa) [49]. This "ultrasoftness" is arguably caused by (i) the much larger mobility and conformational freedom of the single DNA rings within the kDNA and (ii) the larger thickness of kDNA compared with that of typical synthetic 2D materials (approximately nanometers).

The evidence suggesting that the minicircles in the kDNA have valence around 3 is intriguing. A random network with valence 3 is poised near the critical percolation point [25,52,53] yet below the isostatic point for the onset of rigidity [27]. Being poised close to the percolation point ensures that the network is overall connected (thus preserving the integrity of the genome during replication) yet avoids the generation of redundant constraints or a topologically frustrated "overlinked" and rigid network [25]. Perhaps even more intriguingly, the volume fraction of kDNA *in vivo* entails an overlap number $P \simeq 14$, in turn suggesting that kDNA minicircles should display a far larger valence if simply allowed to cross each other freely and randomly. This suggests that the topology of the network is controlled *in vivo*. In this respect, packaging proteins such as KAP and controlling temporal and/or spatial activity of topoisomerase may play a key role [19].

We also mention that, although different species of trypanosomes have different kDNA structures, they all display an overall percolating network. We argue that species with longer minicircles should display an even larger valence, scaling as $v \sim \rho L^{3v-1}$ [54,55] with $\nu = 1/2$ for short rings and $\nu = 1/3$ for longer flexible rings [56]. If this were not to be the case, it would be strong evidence for a biological control of kDNA topology implying an evolutionary benefit in keeping $v \simeq 3$.

In summary, we have here reported a single-molecule high-resolution quantitative analysis of one of the most unique and fascinating genomes in nature. We hope that our work will not only help to unveil the self-assembly and topological regulation of generic kinetoplast DNA networks and their evolutionary pathway, but also provide some insights on how to synthetically design 2D topological soft materials.

IV. METHODS

In order to obtain high-resolution information on the kDNA structure, we perform AFM on kDNA samples purified from *C. fasciculata* (Inspiralis). The kDNA sample is diluted to a concentration of 50–100 ng/μL in a buffer solution containing 50 mM MgCl$_2$; then a droplet of it is deposited onto the mica surface for 1 min followed by 1 mL deionized water flushing and nitrogen blowing. Imaging is performed on a Bruker Multimode AFM in Peakforce-HR mode, using Bruker Scanasyst-air-HR cantilevers with a nominal resonant frequency of 130 kHz and spring constant of 0.4 N/m.

In AFM images, the intensity of the pixel is a direct measure of its height: Brighter pixels correspond to crossings and overlaps of DNA strands. Although the apparent DNA height and width are affected by the tip force, tip radius, and nonhydrated conditions, we use isolated plasmids—similarly affected by artifacts—as a volume reference. Thanks to this feature, we can directly map height to DNA density in each pixel. There can be cases in which DNA strands (about 2–5 nm wide, depending on salt conditions) lay side by side in a 10-nm pixel. In these cases, the intensity of the pixel is not directly proportional to the underlying mass of DNA. The reference volume is measured on isolated plasmids that are much less likely to have multiple strands in one pixel. Therefore, we expect to slightly underestimate the true DNA density in the network.

A. Morphological segmentation

We use MorphoLibJ [57] with no noise reduction and tolerance 15. This plugin uses a modified watershed algorithm to identify objects as basins (the pores) separated by boundaries (the DNA strands). An image with overlaid basins is then generated [see Figs. 5(a) and 5(b)] and analyzed with the "analyze region" function of MorphoLibJ, which returns a list of the values of area, perimeter, circularity, and center of mass of all the basins. The values of pore sizes are then obtained by taking the square root of the areas. The artifacts inside the contour of the kDNA are then removed by identifying the outliers with very large area.

B. Simulations with border constriction

The networks are first built using the NetworkX [39] PYTHON package, and the corresponding meshes are analyzed using libIGL [41] for Python. The networks are built starting from a planar configuration by placing

on half the nodes of the network, corresponding to second neighbors, planar rings and then joining those through the random placement of a set of distorted rings on the remaining nodes. This procedure ensures that the sign of the Hopf link between any two rings is picked randomly between -1 and $+1$, avoiding the onset of topological phenomena such as those reported in Ref. [58]. Using this strategy, we produce three different topologies. The border is then identified with the set of rings that are linked only to two more rings or that are directly linked to one such ring. More details are reported in Supplemental Material [30]. The kDNA minicircles are then modeled as semirigid Kremer-Grest polymers [59] made of $m = 60$ beads having diameter σ and connected by FENE bonds. The rings have persistence length $l_p = 120\sigma$. Each network is a circular hexagonal patch composed by $n = 604$ rings. Different rings interact only by excluded volume, modeled through a Weeks-Chandler-Andersen potential. The system is evolved using an underdamped Langevin dynamics with time step $dt = 0.01\tau_{LJ}$ and damping $\gamma = 0.1\tau_{LJ}^{-1}$, where τ_{LJ} is the characteristic time of the simulation. At each time step, we impose the constraint potential $V_{constr} = K(R_g - R_{g,hc})^2$. These simulations are performed in LAMMPS [40]. The codes can be found open source [60].

C. AFM-steered simulations

Briefly, we model kDNA minicircles as bead-spring polymers with a persistence length of 50 nm. Each bead is given a size equal to that of the resolution of the pixel, i.e., $\sigma = 10$ nm. The AFM image is transformed (see the main text and Supplemental Material [30]) into a series of phantom, static beads that act as attractors of the DNA beads. The system is evolved using a velocity-Verlet algorithm and Langevin dynamics (implicit solvent) with time step $dt = 0.01\tau_{Br}$, where $\tau_{Br} = \gamma\sigma^2/k_BT$ is the Brownian time. For more details on the force fields used, see Supplemental Material [30]. These simulations are also performed in LAMMPS. The codes can be found open source [61].

[1] L. Simpson, *Structure and Function of the Kinetoplast DNA*, J. Protozool. **20,** 2 (1973).

[2] M. Laurent and M. Steinert, *Electron Microscopy of Kinetoplastic DNA from Trypanosoma Mega*, Proc. Natl. Acad. Sci. U.S.A. **66,** 419 (1970).

[3] J. Shlomai and A. Zadok, *Reversible Decatenation of Kinetoplast DNA by a DNA Topoisomerase from Trypanosomatids*, Nucl. Acids Res. **11,** 4019 (1983).

[4] D. L. Pérez-Morga and P. T. Englund, *The Attachment of Minicircles to Kinetoplast DNA Networks during Replication*, Cell **74,** 703 (1993).

[5] J. Shlomai, *The Assembly of Kinetoplast DNA*, Parasitology today **10,** 341 (1994).

[6] J. C. Morris, M. E. Drew, M. M. Klingbeil, S. A. Motyka, T. T. Saxowsky, Z. Wang, and P. T. Englund, *Replication of Kinetoplast DNA: An Update for the New Millennium*, Int. J. Parasitol. **31,** 453 (2001).

[7] J. Lukes, D. Guilbride, and J. Votýpka, *Kinetoplast DNA Network: Evolution of an Improbable Structure*, Eukaryot. Cell **1,** 495 (2002).

[8] L. Simpson and A. da Silva, *Isolation and Characterization of Kinetoplast DNA from Leishmania tarentolae*, J. Mol. Biol. **56,** 443 (1971).

[9] B. Liu, Y. Liu, S. a. Motyka, E. E. C. Agbo, and P. T. Englund, *Fellowship of the Rings: The Replication of Kinetoplast DNA*, Trends Parasitol. **21,** 363 (2005).

[10] M. M. Klingbeil, M. E. Drew, Y. Liu, J. C. Morris, S. A. Motyka, T. T. Saxowsky, Z. Wang, and P. T. Englund, *Unlocking the Secrets of Trypanosome Kinetoplast DNA Network Replication*, Protistologica **152,** 255 (2001).

[11] A. Hoffmann, S. Käser, M. Jakob, S. Amodeo, C. Peitsch, J. Týc, S. Vaughan, B. Zuber, A. Schneider, and T. Ochsenreiter, *Molecular Model of the Mitochondrial Genome Segregation Machinery in Trypanosoma brucei*, Proc. Natl. Acad. Sci. U.S.A. **115,** E1809 (2018).

[12] A. Kalichava and T. Ochsenreiter, *Ultrastructure Expansion Microscopy in Trypanosoma brucei*, Open Biol. **11,** 14 (2021).

[13] A. Schnaufer, *Evolution of Dyskinetoplastic Trypanosomes: How, and How Often?*, Trends Parasitol. **26,** 557 (2010).

[14] A. R. Klotz, B. W. Soh, and P. S. Doyle, *Equilibrium Structure and Deformation Response of 2D Kinetoplast Sheets*, Proc. Natl. Acad. Sci. U.S.A. **117,** 121 (2020).

[15] B. W. Soh, A. Khorshid, D. Al Sulaiman, and P. S. Doyle, *Ionic Effects on the Equilibrium Conformation of Catenated DNA Networks*, Macromolecules **53,** 8502 (2020).

[16] B. W. Soh and P. S. Doyle, *Equilibrium Conformation of Catenated DNA Networks in Slitlike Confinement*, ACS Macro Lett. **10,** 880 (2021).

[17] A. H. Fairlamb, P. O. Weislogel, J. H. Hoeijmakers, and P. Borst, *Isolation and Characterization of Kinetoplast DNA from Bloodstream Form of Trypanosoma brucei*, J. Cell Biol. **76,** 293 (1978).

[18] D. P. Cavalcanti, D. L. Gonçalves, L. T. Costa, and W. de Souza, *The Structure of the Kinetoplast DNA Network of Crithidia fasciculata Revealed by Atomic Force Microscopy*, Micron **42,** 553 (2011).

[19] N. Yaffe, D. Rotem, A. Soni, D. Porath, and J. Shlomai, *Direct Monitoring of the Stepwise Condensation of Kinetoplast DNA Networks*, Sci. Rep. **11,** 1 (2021).

[20] D. C. Barker, *The Ultrastructure of Kinetoplast DNA with Particular Reference to the Interpretation of Dark Field Electron Microscopy Images of Isolated, Purified Networks*, Micron **11**, 21 (1980).

[21] J. Chen, C. A. Rauch, J. H. White, P. T. Englund, and N. Cozzarelli, *The Topology of the Kinetoplast DNA Network*, Cell **80**, 61 (1995).

[22] J. Chen, P. T. Englund, and N. R. Cozzarelli, *Changes in Network Topology during the Replication of Kinetoplast DNA*, EMBO J. **14**, 6339 (1995).

[23] L. Ibrahim, P. Liu, M. Klingbeil, Y. Diao, and J. Arsuaga, *Estimating Properties of Kinetoplast DNA by Fragmentation Reactions*, J. Phys. A **52**, 034001 (2019).

[24] Y. Diao, K. Hinson, R. Kaplan, M. Vazquez, and J. Arsuaga, *The Effects of Density on the Topological Structure of the Mitochondrial DNA from Trypanosomes*, J. Math. Biol. **64**, 1087 (2012).

[25] D. Michieletto, D. Marenduzzo, and E. Orlandini, *Is the Kinetoplast DNA a Percolating Network of Linked Rings at Its Critical Point?*, Phys. Biol. **12**, 036001 (2015).

[26] L. E. Silver, A. F. Torri, and S. L. Hajduk, *Organized Packaging of Kinetoplast DNA Networks*, Cell **47**, 537 (1986).

[27] J. Maxwell, *L. On the Calculation of the Equilibrium and Stiffness of Frames*, Philos. Mag. **27**, 294 (1864).

[28] S. Shankar and D. R. Nelson, *Thermalized Buckling of Isotropically Compressed Thin Sheets*, Phys. Rev. E **104**, 054141 (2021).

[29] D. Wirtz, *Particle-Tracking Microrheology of Living Cells: Principles and Applications*, Annu. Rev. Biophys. **38**, 301 (2009).

[30] See Supplemental Material at http://link.aps.org/supplemental/10.1103/PhysRevX.13.021010 for simulation and experimental details and two videos from simulations.

[31] J. M. Polson, E. J. Garcia, and A. R. Klotz, *Flatness and Intrinsic Curvature of Linked-Ring Membranes*, Soft Matter **17**, 10505 (2021).

[32] G. Witz, K. Rechendorff, J. Adamcik, and G. Dietler, *Conformation of Circular DNA in Two Dimensions*, Phys. Rev. Lett. **101**, 148103 (2008).

[33] C. Rivetti, M. Guthold, and C. Bustamante, *Scanning Force Microscopy of DNA Deposited onto Mica: Equilibrium versus Kinetic Trapping Studied by Statistical Polymer Chain Analysis*, J. Mol. Biol. **264**, 919 (1996).

[34] D. Perez-Morga and P. T. Englund, *The Structure of Replicating Kinetoplast DNA Networks*, J. Cell Biol. **123**, 1069 (1993).

[35] C. A. Rauch, D. Perez-Morga, N. Cozzarelli, and P. T. Englund, *The Absence of Supercoiling in Kinetoplast DNA Minicircles*, EMBO J. **12**, 403 (1993).

[36] M. Caraglio, C. Micheletti, and E. Orlandini, *Mechanical Pulling of Linked Ring Polymers: Elastic Response and Link Localisation*, Polymers **9**, 1 (2017).

[37] P. M. Rauscher, S. J. Rowan, and J. J. De Pablo, *Topological Effects in Isolated Poly[n]catenanes: Molecular Dynamics Simulations and Rouse Mode Analysis*, ACS Macro Lett. **7**, 938 (2018).

[38] L. Tubiana, F. Ferrari, and E. Orlandini, *Circular Polycatenanes: Supramolecular Structures with Topologically Tunable Properties*, Phys. Rev. Lett. **129**, 227801 (2021).

[39] A. Hagberg, P. Swart, and D. S Chult, *Exploring Network Structure, Dynamics, and Function Using NetworkX, technical report, Los Alamos National Lab, Los Alamos, NM*, 2008.

[40] S. Plimpton, *Fast Parallel Algorithms for Short-Range Molecular Dynamics*, J. Comput. Phys. **117**, 1 (1995).

[41] X. Fang, M. Desbrun, H. Bao, and J. Huang, *Topocut: Fast and Robust Planar Cutting of Arbitrary Domains*, ACM Trans. Graph. **41**, 1 (2022).

[42] D. Legland, I. Arganda-Carreras, and P. Andrey, *MorphoLibJ: Integrated Library and Plugins for Mathematical Morphology with ImageJ*, Bioinformatics **32**, 3532 (2016).

[43] N. Conrad, T. Kennedy, D. K. Fygenson, and O. A. Saleh, *Increasing Valence Pushes DNA Nanostar Networks to the Isostatic Point*, Proc. Natl. Acad. Sci. U.S.A. **116**, 7238 (2019).

[44] A. Sharma, A. J. Licup, K. A. Jansen, R. Rens, M. Sheinman, G. H. Koenderink, and F. C. Mackintosh, *Strain-Controlled Criticality Governs the Nonlinear Mechanics of Fibre Networks*, Nat. Phys. **12**, 584 (2016).

[45] M. Wyart, H. Liang, A. Kabla, and L. Mahadevan, *Elasticity of Floppy and Stiff Random Networks*, Phys. Rev. Lett. **101**, 215501 (2008).

[46] A. Zaccone and E. Scossa-Romano, *Approximate Analytical Description of the Nonaffine Response of Amorphous Solids*, Phys. Rev. B **83**, 184205 (2011).

[47] A. Janshoff and C. Steinem, *Mechanics of Lipid Bilayers: What Do We Learn from Pore-Spanning Membranes?*, Biochim. Biophys. Acta **1853**, 2977 (2015).

[48] Z. Chen, D. Wan, and M. J. Bowick, *Spontaneous Tilt of Single-Clamped Thermal Elastic Sheets*, Phys. Rev. Lett. **128**, 028006 (2022).

[49] D. Zhao, Z. Zhang, J. Zhao, K. Liu, Y. Liu, G. Li, X. Zhang, R. Bai, X. Yang, and X. Yan, *A Mortise-and-Tenon Joint Inspired Mechanically Interlocked Network*, Angew. Chem., Int. Ed. **60**, 16224 (2021).

[50] D. P. August, R. A. Dryfe, S. J. Haigh, P. R. Kent, D. A. Leigh, J. F. Lemonnier, Z. Li, C. A. Muryn, L. I. Palmer, Y. Song, G. F. Whitehead, and R. J. Young, *Self-Assembly of a Layered Two-Dimensional Molecularly Woven Fabric*, Nature (London) **588**, 429 (2020).

[51] R. Li, H. Chen, and J. H. Choi, *Auxetic Two-Dimensional Nanostructures from DNA***, Angew. Chem., Int. Ed. **60**, 7165 (2021).

[52] Y. Diao, K. Hinson, and J. Arsuaga, *The Growth of Minicircle Networks on Regular Lattices*, J. Phys. A **45**, 035004 (2012).

[53] Y. Diao, V. Rodriguez, M. Klingbeil, and J. Arsuaga, *Orientation of DNA Minicircles Balances Density and Topological Complexity in Kinetoplast DNA*, PLoS One **10**, 1 (2015).

[54] M. Cates and J. Deutsch, *Conjectures on the Statistics of Ring Polymers*, J. Phys. (Paris) **47**, 2121 (1986).

[55] T. A. Vilgis and M. Otto, *Elasticity of Entangled Polymer Loops: Olympic Gels*, Phys. Rev. E **56**, R1314 (1997).

[56] J. D. Halverson, W. B. Lee, G. S. Grest, A. Y. Grosberg, and K. Kremer, *Molecular Dynamics Simulation Study of Nonconcatenated Ring Polymers in a Melt. I. Statics*, J. Chem. Phys. **134**, 204904 (2011).

[57] D. Legland, I. Arganda-Carreras, and P. Andrey, *Morpho-LibJ: Integrated Library and Plugins for Mathematical Morphology with ImageJ*, Bioinformatics **32**, 3532 (2016).

[58] L. Tubiana, F. Ferrari, and E. Orlandini, *Circular Polycatenanes: Supramolecular Structures with Topologically Tunable Properties*, Phys. Rev. Lett. **129**, 227801 (2022).

[59] K. Kremer and G. S. Grest, *Dynamics of Entangled Linear Polymer Melts: A Molecular-Dynamics Simulation*, J. Chem. Phys. **92**, 5057 (1990).

[60] https://github.com/luca-tubiana/kDNA-border-simsURL.

[61] https://git.ecdf.ed.ac.uk/taplab/kdna-afm-mdURL.